Effects of long-range aerosol transport on the microphysical properties of low-level liquid clouds in the Arctic

Q. Coopman[1,2], T. J. Garrett[1], J. Riedi[2], S. Eckhardt[3], and A. Stohl[3]

[1]Department of Atmospheric Sciences, University of Utah, Salt Lake City, UT, USA
[2]Laboratoire d'Optique Atmosphérique, Université de Lille/CNRS, France
[3]Norwegian Institute for Air Research, Kjeller, Norway

Correspondence to: Q. Coopman (quentin.coopman@ed.univ-lille1.fr)

Abstract. The properties of low-level liquid clouds in the Arctic can be altered by long-range pollution transport to the region. Satellite, tracer transport model, and meteorological data sets are used here to determine a Pollution Cloud Interaction (PCI) parameter that expresses the ratio of relative changes in cloud microphysical properties to relative variations in pollution concentrations. For a period between 2008 and 2010, the PCI is calculated as a function of the cloud liquid water path, temperature, altitude, specific humidity, and lower tropospheric stability. For all data, the PCI averages 0.12 ± 0.02 for cloud droplet effective radius and 0.15 ± 0.02 for cloud optical depth. It increases with specific humidity and lower tropospheric stability and is highest when pollution concentrations are low. For a given set of meteorological conditions, we find that the liquid water path of arctic clouds does not respond strongly to pollution, or, not controlling for meteorological state can lead to artificially exaggerated calculations of the PCI magnitude.

1 Introduction

Due to growing concentrations of greenhouse gases and complex feedback processes, the Arctic region has warmed approximately two times faster than the global average (Serreze and Francis, 2006; Serreze et al., 2009; Richter-Menge and Jeffries, 2011), a trend that is anticipated to continue through this century (Yoshimori et al., 2013; Overland and Wang, 2013). Further, the Arctic is not pristine, even if it is remote from industrialized areas and major aerosol sources. Mid-latitude aerosols can be transported to northern latitudes in relatively high concentrations due to low precipitation and strong temperature inversions that inhibit vertical mixing (Sirois and Barrie, 1999; Law and Stohl, 2007; Quinn et al., 2007; Law et al., 2014). From spring to summer, the atmosphere becomes cleaner due to an increase in wet-scavenging (Garrett et al., 2010). The origins of arctic haze tend to be pollution from Eurasia (Shaw, 1995; Stohl, 2006; Shindell et al., 2008; Ancellet et al., 2014), and boreal forest fires in North America, Eastern Europe and Siberia (Stohl, 2006; Stohl et al., 2007).

Such aerosols have the potential to alter cloud properties in the Arctic (Garrett and Zhao, 2006; Lance et al., 2011). On one hand, thin low-level clouds with more numerous smaller droplets can radiate more long wave radiation thereby warming the surface (Garrett et al., 2002, 2004; Garrett and Zhao, 2006). On the other, polluted clouds can reflect more sunlight, leading to a cooling effect (Lubin and Vogelmann, 2007). Zhao and Garrett (2015) found that seasonal changes in surface radiation associated with haze pollution range from $+12.2\,\mathrm{W\,m^{-2}}$ in February to $-11.8\,\mathrm{W\,m^{-2}}$ in August. Annually averaged, the longwave warming and shortwave cooling nearly compensate, although the seasonal timing of the forcings may have implications for rates of sea ice melt (Belchansky et al., 2004; Markus et al., 2009).

The Influence of aerosols on cloud microphysical properties is often quantified using an indirect-effect (IE) or aerosol-cloud interactions (ACI) parameter that expresses the ratio of relative changes in cloud microphysical properties to variations in pollution concentrations, most typically aerosol index, the aerosol optical depth, the aerosol concentration, or the cloud condensation nucleus (CCN) concentration (Feingold et al., 2001; Feingold; 2003b). Where a parameter is expected to decrease with increasing aerosols or cloud condensation nuclei (e.g. the effective radius), the ratio is multiplied by negative one so that the IE or ACI is positive.

Garrett et al. (2004) used ground-based measurements of the cloud-droplet effective radius and dried aerosol light scattering at Barrow (Alaska) to retrieve an indirect-effect value for the cloud-droplet effective radius between 0.13 and 0.19. Satellite measurements show that IE values for cloud-droplet effective radius range from 0.02 to 0.20 for mid-latitude continental clouds (Nakajima et al., 2001; Feingold, 2003a; Lohmann and Feichter, 2005; Myhre et al., 2007) and from 0.03 to 0.15 for mid-latitude oceanic clouds (Bréon et al., 2002; Sekiguchi, 2003; Kaufman et al., 2005; Myhre et al., 2007; Costantino and Bréon, 2013; Wang et al., 2014). Satellite instruments have the advantage of providing data over large spatial scales, however satellite retrievals of aerosol concentrations are normally obtained from air columns close to the analyzed cloud. The assumption is made that plumes are horizontally homogeneous both within and without the cloud, and that they are vertically co-located with cloud top (Nakajima et al., 2001; Feingold et al., 2001; Sekiguchi, 2003). For large-scale cloud studies, this method potentially introduces bias since it is not obvious that pollution should be uniform for different meteorological regimes.

Co-locating satellite cloud retrievals with pollution tracer output from a chemical transport model offers an alternative approach for assessing the effect of pollution on clouds. In this way, cloud microphysical properties and pollution concentrations can be estimated at the same time, location, and meteorological regime (Schwartz et al., 2002; Kawamoto et al., 2006; Avey et al., 2007). Active tracers experience both sources and sinks, for example through wet scavenging, dry deposition, and chemical reactions. Passive pollution tracers, on the other hand, are determined only by their source and subsequent dilution. An example of a passive tracer is carbon monoxide (CO), which is a combustion by-product and correlates with the anthropogenic CCN close to pollution sources (Longley et al., 2005). Passive tracers are decoupled from clouds and are unaffected by wet scavenging, so what can be expressed is the orthogonal sensitivity of clouds to pollution in a manner that accounts for the possibility of aerosol removal. In the absence of wet scavenging, a linear relation exists between aerosols and a passive tracer since both are a by-product of combustion (Longley et al., 2005). Under these conditions relatives changes in either quantity should be expected to be similar. If, however, aerosols are scavenged during long-range transport, then the cloud sensitivity to pollution is low even if the sensitivity to aerosols remains high.

Most generally, the primary control on cloud microphysical properties is not aerosols but rather meteorological conditions during cloud formation (Chang and Coakley, 2007; Brenguier and Wood, 2009; Kim et al., 2008; Painemal et al., 2014; Andersen and Cermak, 2015). For example, a reduced stability of the environmental temperature profile can allow for enhanced cloud-droplet growth through increasing convection (Klein and Hartmann, 1993). This would be expected to lead to greater mixing of the aerosols with the cloudy air and greater aerosol impacts on cloud microphysical properties (Chen et al., 2014;

Andersen and Cermak, 2015). Also, in the Arctic during the winter, pollution plumes from Asia are often associated with higher values of potential temperature than pollution plumes from Europe (Stohl, 2006). Thus, the observed impact of pollution plumes on clouds may be correlated with a particular meteorological regime.

Using the approach of co-locating a passive CO tracer from a tracer transport model and satellite observations, Tietze et al. (2011) presented an analysis of pollution-cloud interactions over the Arctic from March to July 2008. Anthropogenic and biomass burning pollution was represented with a CO passive tracer in the FLEXPART (FLEXible PARTicle dispersion model) tracer model (Stohl et al., 2005) and was co-located with POLDER-3 (Polarization and Directionality of the Earth's Reflectance) and MODIS (Moderate Resolution Imaging Spectroradiometer) observations. Tietze et al. (2011) showed that the sensitivity of liquid cloud effective radius (r_e) and optical depth (τ) to pollution has a maximum around the freezing point, and that the sensitivity decreases for both higher and lower temperatures. The optical depth was generally up to four times more sensitive than the effective radius. Their results also suggested that biomass burning pollution has a smaller yet significant impact on liquid cloud microphysical properties than anthropogenic pollution, and that the IE parameters depend on altitude, LWP, and temperature.

Our study extends the Tietze et al. (2011) research by adding two years of data, 2009 and 2010 and, in addition to temperature, by controlling for lower tropospheric stability (LTS) and atmospheric specific humidity (Matsui et al., 2006; Mauger and Norris, 2007). Our results highlight the importance of considering meteorological conditions when assessing the aerosol impact on cloud microphysical properties to show that r_e and τ have similar sensitivities to pollution.

2 Data

The analyses in this study are based on a co-location of satellite retrievals of cloud properties, tracer transport model simulations of pollution locations and concentrations, and reanalysis data sets for meteorological fields.

2.1 Satellite cloud property retrievals

In this study we used two instruments, both part of the A-train mission (Stephens et al., 2002). The MODIS instrument on board the Aqua satellite measures radiation in 36 different spectral bands with central wavelength from 400 nm to 14 400 nm in wavelength. For the effective radius, optical depth, and cloud top temperature we use Collection 5 Level-2 products (Platnick et al., 2003; King and Platnick, 2006). Regarding the technique applied for computation of the MODIS Level-2 products cloud top temperature is derived from the 11 µm infrared band. Cloud-droplet effective radius (r_e) and optical depth (τ) are retrieved from simultaneous cloud-reflectance measurements in three water absorbing bands (1.6, 2.1, 3.7 µm) and three non-absorbing bands (0.65, 0.86, 1.2 µm) (Platnick et al., 2003). The pixel resolution of the retrievals at nadir is 1 km×1 km for cloud microphysics and 5 km×5 km for cloud top temperature.

The POLDER-3 camera on the PARASOL satellite platform (Polarization & Anisotropy of Reflectances for Atmospheric Sciences coupled with Observations from a Lidar) captures a wide field of view through spectral, directional, and polarized measurements of reflected sunlight (Fougnie et al., 2007). Multidirectional observations allow for a pixel to be observed from up to sixteen different view angles. The instrument measures radiance in 9 spectral channels between 443 and 1020 nm, including three polarized channels at 490, 670 and 865 nm. POLDER-3 cloud microphysical properties retrievals have a $36\,\mathrm{km}\times 36\,\mathrm{km}$ spatial resolution. Cloud top pressure is derived from the cloud oxygen pressure (Bréon and Colzy, 1999). Cloud top pressure retrieved by POLDER-3 appears to be a better proxy for low-level cloud height than MODIS cloud top pressure derived using a thermal signature assuming a given temperature profile (Buriez et al., 1997; Weisz et al., 2007; Tietze et al., 2011; Desmons et al., 2013).

To determine the cloud thermodynamic phase we use a combination of MODIS and POLDER-3 measurements. The algorithm takes advantage of multi-angle polarization data, shortwave, thermal infrared, and visible measurements to retrieve a thermodynamic phase index Φ between 0 for liquid clouds and 200 for ice clouds with varying degrees of confidence (Riedi et al., 2010). Figure 1 shows the distribution of the thermodynamic phase index for clouds between 200 and 1000 m and between 1000 and 2000 m altitude from 2008 to 2010 over a region with latitudes greater than 65°. We observe different modes in the phase index corresponding to liquid clouds with Φ lower than 70, clouds with undetermined phase, mixed phase or multiple cloud layers, for which Φ lies between 70 and 140, and ice clouds with Φ greater than 140.

2.2 Anthropogenic pollution tracer fields

For determining anthropogenic pollution tracer fields, we used the Lagrangian particle dispersion model FLEXPART (Stohl et al., 1998, 2005). The model is driven with 3 hourly operational analysis wind fields from the European Centre for Medium-Range Weather Forecasts (ECMWF) with 91 model levels and a horizontal resolution of $1^\circ\times 1^\circ$. We used the same simulations as described by Stohl et al. (2013), which considered a black-carbon tracer undergoing removal processes, two fixed-lifetime black carbon tracers, and a carbon monoxide (CO) tracer. The CO tracer used for this study was considered as passive in the atmosphere but was removed from the simulation 31 days after emission, thus focussing the simulation on "fresh" pollution. For the CO emission, ECLIPSE (Evaluating the CLimate and Air Quality ImPacts of Short-livED Pollutants) version 4.0 emission data (Klimont et al., 2015; Stohl et al., 2015) were used. For the anthropogenic emissions considered here, the ECLIPSE emissions are based on the GAINS (Greenhouse gas – Air pollution Interactions and Synergies) model (Amann et al., 2011). The emissions were determined separately for every year of this study and, notably, include gas flaring emissions, which were shown to be important for black carbon in the Arctic (Stohl et al., 2013). Emissions from the residential sector were temporally disaggregated using a heating degree day approach (Stohl et al., 2013).

Studies that have used FLEXPART CO concentration fields (χ_{CO}) have found satisfactory agreement between model output and measurements (Stohl, 2006; Paris et al., 2009; Hirdman et al., 2010; Sodemann et al., 2011; Stohl et al., 2013, 2015; Eckhardt et al., 2015). In the Alaskan Arctic for the day of 18 April 2008, Warneke et al. (2009) described a slope of 0.9 for a linear fit between FLEXPART model output of χ_{CO} and airborne measurements of CO with a least-squares correlation coefficient of 0.63.

The FLEXPART model outputs used here have a temporal resolution of 3 h and a spatial resolution of $1^\circ\times 2^\circ$ (in latitude and longitude) divided into 9 different vertical levels. FLEXPART CO concentration (χ_{CO}) output is provided in units of $\mathrm{mg\,m^{-3}}$ but converted to units of ppbv (parts per billion by volume) to remove the atmospheric pressure dependence. Since the focus here is on the effect of anthropogenic pollution on clouds, only FLEXPART spatial bins where anthropogenic sources comprise more than 80 % of total CO concentrations are considered for comparison with cloud properties.

2.3 Meteorological data

ERA-Interim (ERA-I) reanalysis data from ECMWF (Berrisford et al., 2009) extends from 1989 to the present with an improved version released in 2011 (Dee et al., 2011). The temporal resolution is 6 h at 60 pressure levels. Reanalysis data from ERA-I shows good agreement with satellite retrievals and aircraft data for cloud fraction and cloud radiative forcing in the Arctic (Zygmuntowska et al., 2012). Wesslén et al. (2014) analyzed ERA-I data with the Arctic Cloud-Ocean Study (ASCOS) campaign measurements in 2008 and calculated biases of about 1.3 °C, 1 % and $-1.5\,\mathrm{hPa}$ respectively for temperature, relative humidity and surface pressure, root mean square errors of about 1.9 °C, 3.7 % and 8.7 hPa respectively, and correlation coefficients of approximately 0.85 for temperature and surface pressure and 0.31 for the relative humidity.

The goal of this study is to use satellite, tracer transport model, and meteorological data sets to determine the effects of pollution on cloud microphysics due only to pollution itself and not to the meteorological state. The focus is on temperature, specific humidity, and LTS since these have been identified as a basic meteorological quantities that correlate with cloud microphysical properties (Matsui et al., 2006; Mauger and Norris, 2007). Defining the potential temperature (θ) as

$$\theta = T \cdot \left(\frac{P_0}{P}\right)^{\frac{R}{c_p}} \tag{1}$$

where T and P are the air temperature and pressure, P_0 equals 1000 hPa and R, and c_p are respectively the gas constant for air, and the isobaric heat capacity, the LTS is defined as the potential temperature difference between 700 and 1000 hPa (Klein and Hartmann, 1993).

$$\mathrm{LTS} = \theta_{700} - \theta_{1000} \tag{2}$$

We also consider clouds with values of LWP greater than $40\,\mathrm{g\,m^{-2}}$ separately from clouds with LWP values less than $40\,\mathrm{g\,m^{-2}}$. This approach separates clouds according to their thermal radiative properties since a cloud with low LWP will tend to act as a graybody and potentially be more radiatively susceptible to pollution in the thermal infrared (Garrett and Zhao, 2006; Lubin and Vogelmann, 2006; Mauritsen et al., 2011). Thick clouds act as blackbodies, and their longwave radiative properties are determined by temperature only (Garrett and Zhao, 2006; Garrett et al., 2009).

The different data sets used in this article are summarized in Table 1.

3 Methodology

This study examines data between 2008 and 2010 over the ocean at latitudes greater than 65°. Passive satellite sensors an interaction of solar radiation with the atmosphere to retrieve cloud microphysical parameters of interest from visible wavelength measurements so analyses are restricted to the period between 1 March and 30 September.

3.1 Co-location of satellite retrieval and model pollution tracer fields

CO tracer concentrations from a FLEXPART grid cell are defined as the average between two temporal points, averaged over a spatial box. For example, model CO concentrations at 03:00 UTC and at the latitude–longitude co-ordinates of (70°, 80°), represent an average over a box between the latitudes of 70 to 71° and longitudes of 80 to 82° and between 00:00 UTC and 03:00 UTC.

For an A-train satellite overpass time of 00:45 UTC, we match space-based retrievals to FLEXPART concentration output at 03:00 UTC representing the average concentration between 00:00 UTC to 03:00 UTC and then linearly interpolate ECMWF meteorological fields to the LTS and specific humidity values for 01:30 UTC.

Here, as with many prior studies looking at aerosol-cloud interactions in the Arctic, we consider only low-level clouds (Garrett et al., 2004; Garrett and Zhao, 2006; Lubin and Vogelmann, 2006; Mauritsen et al., 2011), with POLDER cloud top altitudes between 200 and 1000 m, and between 1000 and 2000 m. The cloud top pressure is translating to cloud top altitude by a pressure profile specific to the Arctic region. These two layers correspond to the FLEXPART vertical bin resolution. We average POLDER and MODIS data that falls within the height bins so they are co-located with the corresponding FLEXPART CO concentrations.

Regarding horizontal co-location, Fig. 2 shows how the datasets are combined. We project data from satellite, model, and reanalysis data sets onto an equal-area sinusoidal grid such that the grid-cell resolution is $0.5° \times 0.5°$ at the equator corresponding to an area of $54\,\mathrm{km} \times 54\,\mathrm{km}$. The sinusoidal projection conserves the grid-cell area independently of longitude and latitude. One grid-cell can include up to 81 POLDER-MODIS pixels. Satellite and tracer transport model data are averaged over each grid-cell.

One consequence of the averaging is that each grid-cell can include up to 81 different pixel-level values of Φ. We place a limit on the SD of the averaged phase index within each grid-cell such that $\sigma_\Phi < 10$ in order to satisfy an a priori requirement of there being a nearly homogeneous phase within each grid cell.

3.2 The indirect-effect parameter

Assuming a constant LWC and a mono-disperse size distribution of cloud droplets, the droplet effective radius (r_e) decreases as the droplet number concentration N_c increases following the relation (Feingold et al., 2001):

$$\frac{\partial \ln r_\mathrm{e}}{\partial \ln N_\mathrm{c}}\Big|_{\mathrm{LWP}} = -\frac{1}{3} \tag{3}$$

Here, we take a different approach which is to examine the sensitivity of clouds properties to the CO tracer under the presumption that the CO tracer serves as a proxy for the potential of pollution, of which CCN may be a part, to modify N_c. Of course, N_c and CO tracer concentrations (χ_{CO}) do not represent the same quantity. However, cloud condensation nuclei and CO are both by-products of combustion. The two quantities are expected to be highly correlated close to pollution sources (Avey et al., 2007; Tietze et al., 2011). We do not directly consider the effect of CCN or aerosols on clouds but rather the extent to which a pollution plume interacts with cloud microphysical properties. Often what is evaluated is aerosol-cloud interactions (or ACI). However, if aerosols have been scavenged en route to the Arctic then pollution may be present but its impact on cloud properties weak. Thus, we employ the term PCI instead for pollution-cloud interactions. Thus, interactions between pollution and clouds can be expressed alternatively as:

$$\mathrm{PCI}_{\tau} = \frac{\mathrm{d}\ln\tau}{\mathrm{d}\ln\chi_{\mathrm{CO}}} \tag{4}$$

$$\mathrm{PCI}_{r_\mathrm{e}} = -\frac{\mathrm{d}\ln r_\mathrm{e}}{\mathrm{d}\ln\chi_{\mathrm{CO}}} \tag{5}$$

For example, if N_c, from Eq. (3) is linearly related with χ_{CO} then Eq. (5) has as its theoretical maximum value of $\mathrm{PCI}_{r_\mathrm{e}} = 1/3$ (Twomey, 1977; Feingold et al., 2001).

Further from source regions, the correlation of CO concentration and aerosols is invariant to dilution but is sensitive to wet and dry scavenging (Garrett et al., 2010, 2011). When aerosol scavenging rates are low, CO and CCN will tend to covary. Values of PCI tend to be lower when precipitation is high along transport pathways and aerosols are removed. Garrett et al. (2010) found that at Barrow, Alaska, when the temperature exceeds 4 °C at the surface, wet scavenging efficiently removes CCN from the atmosphere and cloud microphysical properties are not affected by pollution even if the CO remains. Moreover, the simulated CO tracer by the transport model FLEXPART can be de-correlated from the real pollution loading, which can introduce scatter in the results presented here. Effectively, what is expressed by Eq. (4) and (5) is not the sensitivity of clouds to aerosols, but rather their sensitivity to pollution, taking into account the possibility that the CCN of the polluted air parcel may have been removed. The analysis becomes less focussed on the local physics and more focused on the actual impact of anthropogenic activities on clouds far from the combustion source.

Since r_e and the optical depth (τ) are linked through $\tau = \frac{3}{2}\frac{LWP}{\rho_\mathrm{w} r_\mathrm{e}}$ it follows that

$$\frac{\partial\ln\tau}{\partial\ln\chi_{\mathrm{CO}}} = -\frac{\partial\ln r_\mathrm{e}}{\partial\ln\chi_{\mathrm{CO}}} + \frac{\partial\ln\mathrm{LWP}}{\partial\ln\chi_{\mathrm{CO}}} \tag{6}$$

or,

$$\mathrm{PCI}_{\tau} = \mathrm{PCI}_{r_\mathrm{e}} + \mathrm{PCI}_{\mathrm{LWP}} \tag{7}$$

Figure 3 shows an PCI retrieval example for temperatures between -12 and 6 °C and altitudes between 1000 and 2000 m, for all LWP values. We first calculate $\mathrm{PCI}_{r_\mathrm{e}}$ as the linear fit of the natural logarithm of the effective radius to the natural logarithm of CO concentrations. The fit used in this study is based on the robust linear method (RLM) (Huber, 1973, 1981; Venables and Ripley, 2013). RLM uses an iterative least squares algorithm: every measurement has initially the same weight; The weights of each point are updated giving a lower weight to points which appear as outliers with respect to the entire dataset. The process iterates several times and stops when the convergence tolerance of the estimated fitting coefficients are below 10^{-8}. The slope is therefore less sensitive to outlier points. In the example of Fig. 3, the slope retrieved by the linear fit is -0.13 ± 0.016. Referring to Eq. (5), $\mathrm{PCI}_{r_\mathrm{e}}$ equals $+0.13 \pm 0.016$.

3.3 Controlling specific humidity and lower tropospheric stability

Figure 4 presents a 2-D histogram of frequency distribution of the specific humidity and the LTS. The LTS ranges from 2.1 to 37 K and the specific humidity from 0.13 to 11 $\mathrm{g\,kg^{-1}}$. The median values for specific humidity and LTS are 2.0 $\mathrm{g\,kg^{-1}}$ and 19 K respectively.

Table 2 describes the method used here to control meteorological conditions. We identify a range in LTS and specific humidity that occupies 15 % of the total space of observed values but that is centered at the mode of the respective distributions. The total LTS range is 2.1 to 37 K, so the interval size is 5.3 K. The specific humidity is distributed over several orders of magnitude. To better represent the distribution, we use a logarithmic scale for this parameter. The logarithm base 10 of specific humidity has an interval of 0.28. The most common values of meteorological state, defined here as the maximum number of measurements, are delimited by the red rectangle in Fig. 4 corresponding to a range between 0.30 and 0.60 for the logarithm of specific humidity, corresponding to a range of 2.0 $\mathrm{g\,kg^{-1}}$ to 4.0 $\mathrm{g\,kg^{-1}}$, and a range of 16.5 K to 21.8 K for LTS. It is these ranges that are focussed upon for calculation of the PCI parameter. We assume these intervals are sufficiently narrow that the variability within the interval has limited impact on cloud microphysics.

4 Results

4.1 Pollution-Cloud Interactions

Figure 5 summarizes PCI values calculated using combined POLDER-3, MODIS, and FLEXPART data for the period between 2008 and 2010 for latitudes greater than 65° over ocean, and control cloud top temperature in bins of 2° between −12 and 6 °C. The results are categorized according to bins in temperature, altitude and LWP, and LTS and specific humidity controlled. The number of grid-cells used to calculate each PCI parameter per bin ranges from 100 to 3300. The PCI parameter is almost always positive but sometimes close to zero. $\mathrm{PCI}_{r_\mathrm{e}}$ ranges from 0 for graybody clouds between 1000 to 2000 m altitude with a cloud top temperature between −6 and −4 °C, to 0.34 for blackbody clouds between 1000 and 2000 m altitude with a cloud top temperature between 4 and 6 °C. PCI_τ ranges from −0.10 for all clouds between 200 and 1000 m altitude with a cloud top temperature of −11 °C, to 0.35 at 3 °C for blackbody clouds between 1000 and 2000 m altitude. In general, PCI_τ and $\mathrm{PCI}_{r_\mathrm{e}}$ are of the same order of magnitude and the maximum values of PCI are found for clouds with temperatures above the freezing temperature.

We define the uncertainty in PCI as the 95 % confidence limit in the calculation of the slope of the linear fit. The uncertainty in the calculated values of $\mathrm{PCI}_{r_\mathrm{e}}$ is generally less than 0.1, except for clouds with temperatures between 4 and 6 °C and between −12 and −10 °C where the uncertainty bar is approximately 0.2. For the optical depth, the uncertainty is typically approximately 0.1, although larger values are observed for high and low cloud top temperatures.

For blackbody clouds between 1000 and 2000 m altitude, the average values of PCI_τ and $\mathrm{PCI}_{r_\mathrm{e}}$ equal 0.20 and 0.14 respectively. For cloud tops between 200 and 1000 m altitude, PCI_τ and $\mathrm{PCI}_{r_\mathrm{e}}$ equal 0.14. For graybody clouds between 1000 and 2000 m, PCI_τ and $\mathrm{PCI}_{r_\mathrm{e}}$ equal 0.12 and 0.08 respectively. For cloud tops between 200 and 1000 m altitude, PCI_τ and $\mathrm{PCI}_{r_\mathrm{e}}$

equals 0.14 and 0.12 respectively. The value of PCI appears to be fairly robust to altitude and cloud thickness and to whether r_e or τ is considered. Table 3 presents the average PCI_τ and $\mathrm{PCI}_{r_\mathrm{e}}$. In all cases, values are near 0.13 ± 0.03.

4.2 Dependence of PCI on pollution concentration, specific humidity, and lower tropospheric stability

Table 4 shows values of $\mathrm{PCI}_{r_\mathrm{e}}$ and PCI_τ for graybody and blackbody clouds, and for $\chi_\mathrm{CO} < 5.5\,\mathrm{ppbv}$ and $\chi_\mathrm{CO} > 10.0\,\mathrm{ppbv}$, corresponding respectively to the lower and upper quartile of CO tracer concentration, and LTS and specific humidity are controlled. For graybody and blackbody clouds, PCI_τ and $\mathrm{PCI}_{r_\mathrm{e}}$ are highest for low values of χ_CO. The difference in PCI values between low and high polluted environments is slightly greater for $\mathrm{PCI}_{r_\mathrm{e}}$ than PCI_τ. Table 4 suggests that cloud effective radius and cloud optical depth are most sensitive to pollution when pollution concentrations are low. Previous studies have hypothesized that the effect of CCN on cloud microphysical properties saturates when cloud-droplet concentrations are high (Bréon et al., 2002; Andersen and Cermak, 2015). This effect does not explain the differences presented in Table 4 because Eq. (4) and (5) already take into account the potential for linear saturation by considering the logarithmic values of χ_CO and cloud parameters.

We now present the sensitivity of the PCI parameter to 5 different ranges of meteorological parameters delimited by the percentiles values presented in Table 5. Figures 6 and 7 show the influence of pollution loading on the cloud-droplet effective radius and cloud optical depth for each of the different specific humidity and LTS regimes. Figure 6 presents the PCI parameter with respect to the cloud optical depth and cloud-droplet effective radius as a function of the specific humidity, controlling LTS according to the method described in Sect. 3.3. Figure 7 is the same as Fig. 6 except that it shows PCI as a function of LTS for a range of specific humidities.

Figure 6 shows that $\mathrm{PCI}_{r_\mathrm{e}}$ and PCI_τ tend to increase with the specific humidity independent of LTS. The PCI parameter is close to zero, or negative, for low values of specific humidity. It increases rapidly with specific humidity, saturating at a maximum value of about $2.5\,\mathrm{g\,kg^{-1}}$. We note that cloud top temperature and specific humidity are weakly correlated. The correlation coefficient (r^2) of the linear regression of the two parameters is 0.20.

$\mathrm{PCI}_{r_\mathrm{e}}$ increases with LTS, from 0.02 for values of LTS ranging between 2.1 and 14 K, to 0.09 for values of LTS between 23 and 38 K. The PCI_τ dependence on LTS is larger: PCI_τ equals 0.10 for LTS values between 2.1 and 14 K and it equals 0.32 for LTS values between 21 and 38 K.

5 Discussion

The results presented here show values of the PCI parameter with respect to the cloud-droplet effective radius and optical depth, for clouds over oceans north of 65° lying between 200 and 2000 m, and for the years between 2008 to 2010. We find PCI values which range from 0.00 to 0.34 for the cloud-droplet effective radius, and from -0.10 to 0.35 for the optical depth.

Prior studies examining the Arctic region have retrieved IE values ranging from -0.10 to 0.40 (Garrett et al., 2004; Lihavainen et al., 2009; Zhao et al., 2012, Sporre et al., 2012). Tietze et al. (2011) calculated IE values ranging from 0.00 to 0.17 using a similar satellite-FLEXPART co-location method. What differs is that we are examining solely anthropogenic pollution, we extend the dataset from one to three years, and we control specific humidity and LTS. The larger PCI values we find in this study suggest a higher sensitivity of cloud microphysical properties to pollution than was found by Tietze et al. (2011).

However, Tietze et al. (2011) also found values of IE_τ that were greater than $\mathrm{IE}_{r_\mathrm{e}}$, by a factor of up to four, and they attributed this difference to unknown dynamic or precipitation feedbacks that make IE_LWP greater than zero (Eq. 7). In contrast, our results show that the $\mathrm{PCI}_{r_\mathrm{e}}$ and PCI_τ parameters are more similar, suggesting no such feedback. Table 6 compares the differences between PCI_τ and $\mathrm{PCI}_{r_\mathrm{e}}$ that are presented in Table 3, along with their corresponding values when specific humidity and LTS are not controlled. The difference between $\mathrm{PCI}_{r_\mathrm{e}}$ and PCI_τ is largest when meteorological parameters are not controlled. For all clouds considered, the maximum difference increases from 0.04 when the data are controlled to 0.12 when the data are not controlled. This is important since it suggests that the hypothesized feedbacks discussed by Tietze et al. (2011) may have in fact been due to the natural sensitivity of clouds to local meteorology. Not controlling sufficiently meteorology may lead to artifacts that exaggerate the magnitude of the aerosol indirect effect.

In contrast to most prior efforts, satellite-retrieved cloud properties are not compared to CCN or aerosol concentrations but rather to pollution concentrations – specifically CO simulated from a tracer transport model. For temperatures below $-6\,^\circ$C, low values of PCI are observed. Tietze et al. (2011) hypothesized that at such temperatures, cloud supersaturations may be too small to activate aerosols as CCN or that clouds with lower temperatures have followed longer transport pathways nearer the surface (Stohl, 2006) and therefore had greater exposure to dry deposition.

Table 4 suggests that PCI values are lowest when pollution concentration is high. Figure 8 presents the normalized distribution of potential temperature for polluted and pristine clouds, defined as the upper and lower quartile, for graybody clouds. We present results for graybody clouds because the PCI differences between polluted and clean cases are largest; Results for blackbody and all clouds are not shown here, but have similar results regarding the potential temperature distribution.

Highly polluted air parcels are associated with potential temperatures around 280 K whereas pristine air parcels have a lower potential temperature – around 272 K. We hypothesize that higher values of potential temperature suggest pollution sources from further south, so wet scavenging is more likely to occur during transport and this decreases the correlation between CO tracer and CCN, therefore lowering the PCI parameter. Also, polluted air parcel and aerosols do not necessarily have the same physical and chemical properties at lower and higher latitudes, and this difference may impact the influence of aerosols on cloud microphysics and aerosols (Bilde and Svenningsson, 2004; Dusek et al., 2006; Ervens et al., 2007; Andreae and Rosenfeld, 2008).

In general, we observe that when the moisture increases, the cloud sensitivity to pollution increases. From model simulations based of stratocumulus Ackerman et al. (2004) found that when the relative humidity (RH) above cloud top is high, cloud LWP increases with N_c consistent with theoretical arguments (Albrecht, 1989; Pincus and Baker, 1994), but that when the RH is low, the LWP decreases when N_c increases, as supported by some observations (Coakley and Walsh, 2002). The difference was attributed to the consequence of dry air into a cloud layer. Humidity inversions are common above low-level cloud tops in the Arctic (Nygärd et al., 2014), so similar phenomena may be playing a role.

Studies of the indirect effect at mid-latitudes suggest that values of IE are highest under unstable conditions (Chen et al., 2014; Andersen and Cermak, 2015). Our results show that in the Arctic, the impact of LTS on PCI is the reverse. Klein and

Hartmann (1993) showed that, in general, higher values of LTS lead to greater stratiform cloudiness, except in the Arctic where radiative cooling prevails over convection as the driving mechanism for cloud formation.

Finally, we find PCI_τ is more sensitive to changes in LTS than PCI_{r_e}. A consequence is that for values of LTS greater than 23 K, PCI_τ and PCI_{r_e} differ by about 0.20. In a stable atmosphere with high LTS it appears that $\mathrm{PCI}_{\mathrm{LWP}}$ increases more strongly in response to aerosols than in unstable environments (Klein and Hartmann, 1993; Qiu et al., 2015).

6 Conclusions

Satellite, numerical model, and meteorological reanalysis data sets from 2008 to 2010 were used here to calculate the sensitivity of cloud-droplet effective radius and optical depth in the Arctic to anthropogenic polluted air parcels transported from mid-latitudes. We focused on latitudes north of 65° for the period between March 2008 and October 2010. Using ECMWF reanalysis data, we controlled temperature, LTS, specific humidity, altitude, and LWP for the sensitivity analysis. We find values of PCI close to the theoretical maximum of $1/3$, assuming that a simulated CO tracer correlates well with CCN. PCI_{r_e} and PCI_τ seem to increase with specific humidity and LTS, highlighting that meteorological parameters have an important impact on aerosol-cloud interaction.

Globally, Klimont et al. (2013) have estimated that there was a drop of about 9281 Gg in anthropogenic sulphur dioxide emissions between 2005 and 2010 due to a reduction in European and American emissions and a flue gas desulfurization program on power plants in China. This reduction in emissions has lead to a decrease of sulfate concentrations at Arctic surface station (Hirdman et al., 2010). In the Arctic, the effect of a decrease in mid-latitude pollution emissions may some day be offset by greater levels of Arctic industrialization (Lindholt and Glomsrød, 2012) and shipping (Pizzolato et al., 2014; Miller and Ruiz, 2014) that introduce new local aerosol sources. Further, an increase in the extent of open-ocean due to sea-ice retreat may be expected to lead to an increase in the atmospheric humidity (Boisvert and Stroeve, 2015) and from the results presented here, a higher sensitivity of clouds to aerosols. However, this study also suggests that any associated decrease in LTS may be expected to counter-act this effect. Sea-ice retreat would also enhance dimethyl sulfide emissions, potentially increasing cloud cover in the Arctic (Ji et al., 2013).

Climate warming is thought to stimulate boreal forest fires (Westerling et al., 2006). The impact of pollution from biomass burning has not been included in the present research. Given biomass burning aerosol can act as efficient ice nuclei (Markus et al., 2009), the analyses presented here might be extended to explore aerosol-induced changes in cloud thermodynamic phase.

Acknowledgements. This paper is dedicated posthumously to Kyle Tietze, who developed many of the techniques used in this study while a graduate student at the University of Utah. The authors thank ICARE, NASA and CNES for the data used in this research. We acknowledge financial support from The University of Lille1. This material is based upon work supported by the National Science Foundation under the Grant No. 1303965. NILU researchers have received funding from the European Union Seventh Framework Programme (FP7/2007-2013) under grant agreement no. 282688 – ECLIPSE.

References

Ackerman, A. S., Kirkpatrick, M. P., Stevens, D. E., and Toon, O. B.: The impact of humidity above stratiform clouds on indirect aerosol climate forcing, Nature, 432, 1014–1017, doi:10.1038/nature03137.1, 2004.

Albrecht, B. A.: Aerosols, Cloud Microphysics, and Fractional Cloudiness, Science, 245, 1227–1230, 1989.

Amann, M., Bertok, I., Borken-Kleefeld, J., Cofala, J., Heyes, C., Höglund-Isaksson, L., Klimont, Z., Nguyen, B., Posch, M., Rafaj, P., Sandler, R., Schöpp, W., Wagner, F., and Winiwarter, W.: Cost-effective control of air quality and greenhouse gases in Europe: Modeling and policy applications, Environ. Modell. Softw., 26, 1489–1501, doi:10.1016/j.envsoft.2011.07.012, 2011.

Ancellet, G., Pelon, J., Blanchard, Y., Quennehen, B., Bazureau, A., Law, K. S., and Schwarzenboeck, A.: Transport of aerosol to the Arctic: analysis of CALIOP and French aircraft data during the spring 2008 POLARCAT campaign, Atmos. Chem. Phys., 14, 8235–8254, doi:10.5194/acp-14-8235-2014, 2014.

Andersen, H. and Cermak, J.: How thermodynamic environments control stratocumulus microphysics and interactions with aerosols, Environ. Res. Lett., 10, 24004, doi:10.1088/1748-9326/10/2/024004, 2015.

Andreae, M. O. and Rosenfeld, D.: Aerosol-cloud-precipitation interactions. Part 1. The nature and sources of cloud-active aerosols, Earth-Sci. Rev., 89, 13–41, doi:10.1016/j.earscirev.2008.03.001, 2008.

Avey, L., Garrett, T. J., and Stohl, A.: Evaluation of the aerosol indirect effect using satellite, tracer transport model, and aircraft data from the International Consortium for Atmospheric Research on Transport and Transformation, J. Geophys. Res.-Atmos., 112, 1–10, doi:10.1029/2006JD007581, 2007.

Belchansky, G. I., Douglas, D. C., and Platonov, N. G.: Duration of the Arctic sea ice melt season: Regional and interannual variability, 1979-2001, J. Climate, 17, 67–80, doi:10.1175/1520-0442(2004)017<0067:DOTASI>2.0.CO;2, 2004.

Berrisford, P., Dee, D., Fielding, K., Fuentes, M., Kallberg, P., Kobayashi, S., and Uppala, S.: The ERA-Interim Archive, ECMWF, Reading, UK, 1, available at: http://old.ecmwf.int/publications/library/do/references/list/782009 (last access: 11 November 2015), 2009.

Bilde, M. and Svenningsson, B.: CCN activation of slightly soluble organics: The importance of small amounts of inorganic salt and particle phase, Tellus B, 56, 128–134, doi:10.1111/j.1600-0889.2004.00090.x, 2004.

Boisvert, L. N. and Stroeve, J. C.: The Arctic is becoming warmer and wetter as revealed by the Atmospheric Infrared Sounder, Geophys. Res. Lett., 42, 4439–4446, doi:10.1002/2015GL063775.Received, 2015.

Brenguier, J. and Wood, R.: Observational strategies from the micro to meso scale, in: Clouds in the Perturbed Climate System: Their Relationship to Energy Balance, Atmospheric Dynamics, and Precipitation, edited by: Heintzenberg, J. and Charlson, R. J., 487–510, available at: ftp://ftp-projects.zmaw.de/aerocom/meetings/frankfurt_2007/brenguier.pdf (last access: 11 November 2015), MIT Press, MASS, Cambridge, 2009.

Bréon, F.-M. and Colzy, S.: Cloud detection from the spaceborne POLDER instrument and validation against surface synoptic observations, J. Appl. Meteorol., 38, 777–785, doi:10.1175/1520-0450(1999)038<0777:CDFTSP>2.0.CO;2, 1999.

Bréon, F.-M., Tanré, D., and Generoso, S.: Aerosol effect on cloud droplet size monitored from satellite, Science (New York, N. Y.), 295, 834–8, doi:10.1126/science.1066434, 2002.

Buriez, J. C., Vanbauce, C., Parol, F., Goloub, P., Herman, M., Bonnel, B., Fouquart, Y., Couvert, P., and Seze, G.: Cloud detection and derivation of cloud properties from POLDER, Int. J. Remote Sens., 18, 2785–2813, doi:10.1080/014311697217332, 1997.

Chang, F. L. and Coakley, J. A.: Relationships between marine stratus cloud optical depth and temperature: Inferences from AVHRR observations, J. Climate, 20, 2022–2036, doi:10.1175/JCLI4115.1, 2007.

Chen, Y.-C., Christensen, M. W., Stephens, G. L., and Seinfeld, J. H.: Satellite-based estimate of global aerosol–cloud radiative forcing by marine warm clouds, Nat. Geosci., advance on, 7, 643–646, doi:10.1038/ngeo2214, 2014.

Coakley, J. A. and Walsh, C. D.: Limits to the aerosol indirect radiative effect derived from observations of ship tracks, J. Atmos. Sci., 59, 668–680, doi:10.1175/1520-0469(2002)059<0668:LTTAIR>2.0.CO;2, 2002.

Costantino, L. and Bréon, F. M.: Aerosol indirect effect on warm clouds over South-East Atlantic, from co-located MODIS and CALIPSO observations, Atmos. Chem. Phys., 13, 69–88, doi:10.5194/acp-13-69-2013, 2013.

Dee, D. P., Uppala, S. M., Simmons, A. J., Berrisford, P., Poli, P., Kobayashi, S., Andrae, U., Balmaseda, M. A., Balsamo, G., Bauer, P., Bechtold, P., Beljaars, A. C. M., van de Berg, L., Bidlot, J., Bormann, N., Delsol, C., Dragani, R., Fuentes, M., Geer, A. J., Haimberger, L., Healy, S. B., Hersbach, H., Hólm, E. V., Isaksen, L., Kållberg, P., Köhler, M., Matricardi, M., Mcnally, A. P., Monge-Sanz, B. M., Morcrette, J. J., Park, B. K., Peubey, C., de Rosnay, P., Tavolato, C., Thépaut, J. N., and Vitart, F.: The ERA-Interim reanalysis: Configuration and performance of the data assimilation system, Q. J. Roy. Meteorol. Soc., 137, 553–597, doi:10.1002/qj.828, 2011.

Desmons, M., Ferlay, N., Parol, F., Mcharek, L., and Vanbauce, C.: Improved information about the vertical location and extent of monolayer clouds from POLDER3 measurements in the oxygen A-band, Atmos. Meas. Tech., 6, 2221–2238, doi:10.5194/amt-6-2221-2013, 2013.

Dusek, U., Frank, G. P., Hildebrandt, L., Curtius, J., Schneider, J., Walter, S., Chand, D., Drewnick, F., Hings, S., Jung, D., Borrmann, S., and Andreae, M. O.: Size matters more than chemistry for cloud-nucleating ability of aerosol particles, Science (New York, N. Y.), 312, 1375–1378, doi:10.1126/science.1125261, 2006.

Eckhardt, S., Quennehen, B., Olivié, D. J. L., Berntsen, T. K., Cherian, R., Christensen, J. H., Collins, W., Crepinsek, S., Daskalakis, N., Flanner, M., Herber, A., Heyes, C., Hodnebrog, Ø., Huang, L., Kanakidou, M., Klimont, Z., Langner, J., Law, K. S., Lund, M. T., Mahmood, R., Massling, A., Myriokefalitakis, S., Nielsen, I. E., Nøjgaard, J. K., Quaas, J., Quinn, P. K., Raut, J.-C., Rumbold, S. T., Schulz, M., Sharma, S., Skeie, R. B., Skov, H., Uttal, T., von Salzen, K., and Stohl, A.: Current model capabilities for simulating black carbon and sulfate concentrations in the Arctic atmosphere: a multi-model evaluation using a comprehensive measurement data set, Atmos. Chem. Phys., 15, 9413–9433, doi:10.5194/acp-15-9413-2015, 2015.

Ervens, B., Cubison, M., Andrews, E., Feingold, G., Ogren, J. A., Jimenez, J. L., DeCarlo, P., and Nenes, A.: Prediction of cloud condensation nucleus number concentration using measurements of aerosol size distributions and composition and light scattering enhancement due to humidity, J. Geophys. Res.-Atmos., 112, 1–15, doi:10.1029/2006JD007426, 2007.

Feingold, G.: Modeling of the first indirect effect: Analysis of measurement requirements, Geophys. Res. Lett., 30, 30, 1997, doi:10.1029/2003GL017967, 2003a.

Feingold, G.: First measurements of the Twomey indirect effect using ground-based remote sensors, Geophys. Res. Lett., 30, 19–22, doi:10.1029/2002GL016633, 2003b.

Feingold, G., Remer, L. A., Ramaprasad, J., and Kaufman, Y. J.: Analysis of smoke impact on clouds in Brazilian biomass burning regions: An extension of Twomey's approach, J. Geophys. Res., 106, 22907–22922, 2001.

Fougnie, B., Bracco, G., Lafrance, B., Ruffel, C., Hagolle, O., and Tinel, C.: PARASOL in-flight calibration and performance, Appl. Optics, 46, 5435–5451, doi:10.1364/AO.46.005435, 2007.

Garrett, T. J. and Zhao, C.: Increased Arctic cloud longwave emissivity associated with pollution from mid-latitudes, Letters, 440, 787–789, doi:10.1038/nature04636, 2006.

Garrett, T. J., Radke, L. F., and Hobbs, P. V.: Aerosol Effects on Cloud Emissivity and Surface Longwave Heating in the Arctic, J. Atmos. Sci., 59, 769–778, doi:10.1175/1520-0469(2002)059<0769:AEOCEA>2.0.CO;2, 2002.

Garrett, T. J., Zhao, C., Dong, X., Mace, G. G., and Hobbs, P. V.: Effects of varying aerosol regimes on low-level Arctic stratus, Geophys. Res. Lett., 31, L17105, doi:10.1029/2004GL019928, 2004.

Garrett, T. J., Maestras, M. M., Krueger, S. K., and Shmidt, C. T.: Acceleration by aerosol of a radiative-thermodynamic cloud feedback influencing Arctic surface warming, Geophys. Res. Lett., 36, L19804, doi:10.1029/2009GL040195, 2009.

Garrett, T. J., Zhao, C., and Novelli, P. C.: Assessing the relative contributions of transport efficiency and scavenging to seasonal variability in Arctic aerosol, Tellus B, 62, 190–196, doi:10.1111/j.1600-0889.2010.00453.x, 2010.

Garrett, T. J., Brattström, S., Sharma, S., Worthy, D. E. J., and Novelli, P.: The role of scavenging in the seasonal transport of black carbon and sulfate to the Arctic, Geophys. Res. Lett., 38, L16805, doi:10.1029/2011GL048221, 2011.

Hirdman, D., Sodemann, H., Eckhardt, S., Burkhart, J. F., Jefferson, A., Mefford, T., Quinn, P. K., Sharma, S., Ström, J., and Stohl, A.: Source identification of short-lived air pollutants in the Arctic using statistical analysis of measurement data and particle dispersion model output, Atmos. Chem. Phys., 10, 669–693, doi:10.5194/acp-10-669-2010, 2010.

Huber, P. J.: The 1972 Wald memorial lectures: robust regression: asymptotics, conjectures, and Monte Carlo, The Annals of Statistics, 1, 799–821, 1973.

Huber, P. J.: Robust Statistics, John Wiley and Sons, Inc., New York, 1981.

Ji, R., Jin, M., and Varpe, Ø.: Sea ice phenology and timing of primary production pulses in the Arctic Ocean, Glob. Change Biol., 19, 734–741, doi:10.1111/gcb.12074, 2013.

Kaufman, Y. J., Koren, I., Remer, L. A., Rosenfeld, D., and Rudich, Y.: The effect of smoke, dust, and pollution aerosol on shallow cloud development over the Atlantic Ocean, P. Natl. Acad. Sci. USA, 102, 11207–11212, doi:10.1073/pnas.0505191102, 2005.

Kawamoto, K., Hayasaka, T., Uno, I., and Ohara, T.: A correlative study on the relationship between modeled anthropogenic aerosol concentration and satellite-observed cloud properties over east Asia, J. Geophys. Res.-Atmos., 111, 1–7, doi:10.1029/2005JD006919, 2006.

Kim, B. G., Miller, M. A., Schwartz, S. E., Liu, Y., and Min, Q.: The role of adiabaticity in the aerosol first indirect effect, J. Geophys. Res.-Atmos., 113, 1–13, doi:10.1029/2007JD008961, 2008.

King, M. D. and Platnick, S.: Collection 005 change summary for the MODIS cloud optical property (06 _ OD) algorithm high impact change overview: change details:, Terra, 1, 1–23, 2006.

Klein, S. A. and Hartmann, D. L.: The seasonal cycle of low stratiform clouds, J. Climate, 6, 1587–1606, 1993.

Klimont, Z., Smith, S. J., and Cofala, J.: The last decade of global anthropogenic sulfur dioxide: 2000–2011 emissions, Environ. Res. Lett., 8, 014003, doi:10.1088/1748-9326/8/1/014003, 2013.

Klimont, Z., Hoglund, L., Heyes, C., Rafaj, P., Schoepp, W., Cofala, J., Borken-Kleefeld, J., Purohit, P., Kupiainen, K., Winiwarter, W., Amann, M., Zhao, B., Wang, S. X., Bertok, I., and Sander, R.: Global scenarios of air pollutants and methane: 1990–2050, in preparation, 2015.

Lance, S., Shupe, M. D., Feingold, G., Brock, C. A., Cozic, J., Holloway, J. S., Nenes, A., Schwartz, J. P., Spackman, J. R., Froyd, K. D., Murphy, D. M., Brioude, J., Cooper, O. R., Stohl, A., and Burkhart, J. F.: Cloud condensation nuclei as a modulator of ice processes in Arctic mixed-phase clouds, Atmos. Chem. Phys., 11, 8003–8015, 2011.

Law, K. S. and Stohl, A.: Arctic air pollution: origins and impacts, Science (New York, N. Y.), 315, 1537–40, doi:10.1126/science.1137695, 2007.

Law, K. S., Stohl, A., Quinn, P. K., Brock, C., Burkhart, J., Paris, J. D., Ancellet, G., Singh, H. B., Roiger, A., Schlager, H., Dibb, J., Jacob, D. J., Arnold, S. R., Pelon, J., and Thomas, J. L.: Arctic air pollution: new insights from POLARCAT-IPY, B. Am. Meteorol. Soc., 95, 1873–1895, doi:10.1175/BAMS-D-13-00017.1, 2014.

Lihavainen, H., Kerminen, V. M., and Remer, L. A.: Aerosol-cloud interaction determined by both in situ and satellite data over a northern high-latitude site, Atmos. Chem. Phys., 10, 10987–10995, doi:10.5194/acp-10-10987-2010, 2009.

Lindholt, L. and Glomsrød, S.: The Arctic: No big bonanza for the global petroleum industry, Energ. Econ., 34, 1465–1474, doi:10.1016/j.eneco.2012.06.020, 2012.

Lohmann, U. and Feichter, J.: Global indirect aerosol effects: a review, Atmos. Chem. Phys., 5, 715–737, doi:10.5194/acp-5-715-2005, 2005.

Longley, I. D., Inglis, D. W. F., Gallagher, M. W., Williams, P. I., Allan, J. D., and Coe, H.: Using NO_x and CO monitoring data to indicate fine aerosol number concentrations and emission factors in three UK conurbations, Atmos. Environ., 39, 5157–5169, doi:10.1016/j.atmosenv.2005.05.017, 2005.

Lubin, D. and Vogelmann, A. M.: A climatologically significant aerosol longwave indirect effect in the Arctic, Nature, 439, 453–456, doi:10.1038/nature04449, 2006.

Lubin, D. and Vogelmann, A. M.: Expected magnitude of the aerosol shortwave indirect effect in springtime Arctic liquid water clouds, Geophys. Res. Lett., 34, L11801, doi:10.1029/2006GL028750, 2007.

Markus, T., Stroeve, J. C., and Miller, J.: Recent changes in Arctic sea ice melt onset, freezeup, and melt season length, J. Geophys. Res.-Oceans, 114, 1–14, doi:10.1029/2009JC005436, 2009.

Matsui, T., Masunaga, H., Kreidenweis, S. M., Pielke, R. A., Tao, W. K., Chin, M., and Kaufman, Y. J.: Satellite-based assessment of marine low cloud variability associated with aerosol, atmospheric stability, and the diurnal cycle, J. Geophys. Res.-Atmos., 111, 1–16, doi:10.1029/2005JD006097, 2006.

Mauger, G. S. and Norris, J. R.: Meteorological bias in satellite estimates of aerosol-cloud relationships, Geophys. Res. Lett., 34, 1–5, doi:10.1029/2007GL029952, 2007.

Mauritsen, T., Sedlar, J., Tjernström, M., Leek, C., Martin, M., Shupe, M., Sjogren, S., Sierau, B., Persson, P. O. G., Brooks, I. M., and Swietlicki, E.: An Arctic CCN-limited cloud-aerosol regime, Atmos. Chem. Phys., 11, 165–173, 2011.

Miller, A. W. and Ruiz, G. M.: Arctic shipping and marine invaders, Nature Clim. Change, 4, 413–416, doi:10.1038/nclimate2244, 2014.

Myhre, G., Stordal, F., Johnsrud, M., Kaufman, Y. J., Rosenfeld, D., Storelvmo, T., Kristjansson, J. E., Berntsen, T. K., Myhre, A., and Isaksen, I. S. A.: Aerosol-cloud interaction inferred from MODIS satellite data and global aerosol models, Atmos. Chem. Phys., 7, 3081–3101, doi:10.5194/acp-7-3081-2007, 2007.

Nakajima, T., Higurashi, A., Kawamoto, K., and Penner, J. E.: A possible correlation between satellite-derived cloud and aerosol microphysical parameters, Geophys. Res. Lett., 28, 1171–1174, doi:10.1029/2000GL012186, 2001.

Nygärd, T., Valkonen, T., and Vihma, T.: Characteristics of arctic low-tropospheric humidity inversions based on radio soundings, Atmos. Chem. Phys., 14, 1959–1971, doi:10.5194/acp-14-1959-2014, 2014.

Overland, J. E. and Wang, M.: When will the summer Arctic be nearly sea ice free?, Geophys. Res. Lett., 40, 2097–2101, doi:10.1002/grl.50316, 2013.

Painemal, D., Kato, S., and Minnis, P.: Boundary layer regulation in the southeast Atlantic cloud microphysics during the biomass burning season as seen by the A-train satellite constellation, J. Geophys. Res.-Atmos., 119, 11288–11302, doi:10.1002/2014JD022182, 2014.

Paris, J.-D., Stohl, A., Nédélec, P., Arshinov, M. Yu., Panchenko, M. V., Shmargunov, V. P., Law, K. S., Belan, B. D., and Ciais, P.: Wildfire smoke in the Siberian Arctic in summer: source characterization and plume evolution from airborne measurements, Atmos. Chem. Phys., 9, 9315–9327, doi:10.5194/acp-9-9315-2009, 2009.

Pincus, R. and Baker, M. B.: Effect of precipitation on the albedo susceptibility of clouds in the marine boundary layer, Nature, 372, 250–252, doi:10.1038/372250a0, 1994.

Pizzolato, L., Howell, S. E. L., Derksen, C., Dawson, J., and Copland, L.: Changing sea ice conditions and marine transportation activity in Canadian Arctic waters between 1990 and 2012, Climatic Change, 123, 161–173, doi:10.1007/s10584-013-1038-3, 2014.

Platnick, S., King, M. D., Ackerman, S. A., Menzel, W. P., Baum, B. A., Riédi, J. C., and Frey, R. A.: The MODIS cloud products: Algorithms and examples from terra, IEEE T. Geosci. Remote, 41, 459–472, doi:10.1109/TGRS.2002.808301, 2003.

Qiu, S., Dong, X., Xi, B., and Li, J. F.: Characterizing Arctic mixed-phase cloud structure and its relationship with humidity and temperature inversion using ARM NSA observations, J. Geophys. Res., 120, 7737–7746, doi:10.1002/2014JD023022.Received, 2015.

Quinn, P. K., Shaw, G., Andrews, E., Dutton, E. G., Ruoho-Airola, T., and Gong, S. L.: Arctic haze: Current trends and knowledge gaps, Tellus B, 59, 99–114, doi:10.1111/j.1600-0889.2006.00238.x, 2007.

Richter-Menge, J. and Jeffries, M.: State of the climate in 2010: The Arctic, B. Am. Meteorol. Soc., 92, S143–S160, 2011.

Riedi, J., Marchant, B., Platnick, S., Baum, B. A., Thieuleux, F., Oudard, C., Parol, F., Nicolas, J.-M., and Dubuisson, P.: Cloud thermodynamic phase inferred from merged POLDER and MODIS data, Atmos. Chem. Phys., 10, 11851–11865, 2010.

Schwartz, S. E., Harshvardhan, and Benkovitz, C. M.: Influence of anthropogenic aerosol on cloud optical depth and albedo shown by satellite measurements and chemical transport modeling, P. Natl. Acad. Sci. USA, 99, 1784–1789, doi:10.1073/pnas.261712099, 2002.

Sekiguchi, M.: A study of the direct and indirect effects of aerosols using global satellite data sets of aerosol and cloud parameters, J. Geophys. Res., 108, 1–15, doi:10.1029/2002JD003359, 2003.

Serreze, M. C. and Francis, J. A.: The Arctic on the fast track of change, Weather, 61, 65–69, doi:10.1256/wea.197.05, 2006.

Serreze, M. C., Barrett, A. P., Stroeve, J. C., Kindig, D. N., and Holland, M. M.: The emergence of surface-based Arctic amplification, The Cryosphere, 3, 11–19, doi:10.5194/tc-3-11-2009, 2009.

Shaw, G. E.: The arctic haze phenomenon, B. Am. Meteorol. Soc., 76, 2403–2413, doi:10.1175/1520-0477(1995)076<2403:TAHP>2.0.CO;2, 1995.

Shindell, D. T., Chin, M., Dentener, F., Doherty, R. M., Faluvegi, G., Fiore, A. M., Hess, P., Koch, D. M., MacKenzie, I. A., Sanderson, M. G., Schultz, M. G., Schulz, M., Stevenson, D. S., Teich, H., Textor, C., Wild, O., Bergmann, D. J., Bey, I., Bian, H., Cuvelier, C., Duncan, B. N., Folberth, G., Horowitz, L. W., Jonson, J., Kaminski, J. W., Marmer, E., Park, R., Pringle, K. J., Schroeder, S., Szopa, S., Takemura, T., Zeng, G., Keating, T. J., and Zuber, A.: A multi-model assessment of pollution transport to the Arctic, Atmos. Chem. Phys., 8, 5353–5372, 2008.

Sirois, A. and Barrie, L. A.: Arctic lower tropospheric aerosol trends and composition at Alert, Canada: 1980–1995, J. Geophys. Res., 104, 11599, doi:10.1029/1999JD900077, 1999.

Sodemann, H., Pommier, M., Arnold, S. R., Monks, S. A., Stebel, K., Burkhart, J. F., Hair, J. W., Diskin, G. S., Clerbaux, C., Coheur, P.-F., Hurtmans, D., Schlager, H., Blechschmidt, A.-M., Kristjánsson, J. E., and Stohl, A.: Episodes of cross-polar transport in the Arctic troposphere during July 2008 as seen from models, satellite, and aircraft observations, Atmos. Chem. Phys., 11, 3631–3651, 2011.

Sporre, M. K., Glantz, P., Tunved, P., Swietlicki, E., Kulmala, M., and Lihavainen, H.: A study of the indirect aerosol effect on subarctic marine liquid low-level clouds using MODIS cloud data and ground-based aerosol measurements, Atmos. Res., 116, 56–66, doi:10.1016/j.atmosres.2011.09.014, 2012.

Stephens, G. L., Vane, D. G., Boain, R. J., Mace, G. G., Sassen, K., Wang, Z., Illingworth, A. J., O'Connor, E. J., Rossow, W. B., Durden, S. L., Miller, S. D., Austin, R. T., Benedetti, A., and Mitrescu, C.: The cloudsat mission and the A-Train: A new dimension of space-based observations of clouds and precipitation, B. Am. Meteorol. Soc., 83, 1771–1790+1742, doi:10.1175/BAMS-83-12-1771, 2002.

Stohl, A.: Characteristics of atmospheric transport into the Arctic troposphere, J. Geophys. Res., 111, D11306, doi:10.1029/2005JD006888, 2006.

Stohl, A., Hittenberger, M., and Wotawa, G.: Validation of the lagrangian particle dispersion model FLEXPART against large-scale tracer experiment data, Atmos. Environ., 32, 4245–4264, doi:10.1016/S1352-2310(98)00184-8, 1998.

Stohl, A., Franck, A., Seibert, P., and Wotawa, G.: Technical note: The lagrangian particle dispersion model FLEXPART version 6.2, Atmos. Chem. Phys., 5, 2005.

Stohl, A., Berg, T., Burkhart, J. F., Fjǽraa, A. M., Forster, C., Herber, A., Hov, Ø., Lunder, C., McMillan, W. W., Oltmans, S., Shiobara, M., Simpson, D., Solberg, S., Stebel, K., Ström, J., Tørseth, K., Treffeisen, R., Virkkunen, K., and Yttri, K. E.: Arctic smoke – record high air pollution levels in the European Arctic due to agricultural fires in Eastern Europe in spring 2006, Atmos. Chem. Phys., 7, 511–534, doi:10.5194/acp-7-511-2007, 2007.

Stohl, A., Klimont, Z., Eckhardt, S., Kupiainen, K., Shevchenko, V. P., Kopeikin, V. M., and Novigatsky, A. N.: Black carbon in the Arctic: the underestimated role of gas flaring and residential combustion emissions, Atmos. Chem. Phys., 13, 8833–8855, doi:10.5194/acp-13-8833-2013, 2013.

Stohl, A., Aamaas, B., Amann, M., Baker, L. H., Bellouin, N., Berntsen, T. K., Boucher, O., Cherian, R., Collins, W., Daskalakis, N., Dusinska, M., Eckhardt, S., Fuglestvedt, J. S., Harju, M., Heyes, C., Hodnebrog, Ø., Hao, J., Im, U., Kanakidou, M., Klimont, Z., Kupiainen, K., Law, K. S., Lund, M. T., Maas, R., MacIntosh, C. R., Myhre, G., Myriokefalitakis, S., Olivié, D., Quaas, J., Quennehen, B., Raut, J.-C., Rumbold, S. T., Samset, B. H., Schulz, M., Seland, Ø., Shine, K. P., Skeie, R. B., Wang, S., Yttri, K. E., and Zhu, T.: Evaluating the climate and air quality impacts of short-lived pollutants, Atmos. Chem. Phys., 15, 10529–10566, doi:10.5194/acp-15-10529-2015, 2015.

Tietze, K., Riedi, J., Stohl, A., and Garrett, T. J.: Space-based evaluation of interactions between aerosols and low-level Arctic clouds during the Spring and Summer of 2008, Atmos. Chem. Phys., 11, 3359–3373, 2011.

Twomey, S.: The influence of Pollution on the shortwave Albedo of Clouds, J. Atmos. Sci., 34, 1149–1152,doi:10.1175/1520-0469(1977)034<1149:TIOPOT>2.0.CO;2 1977.

Venables, W. N. and Ripley, B. D.: Modern Applied Statistics with S-PLUS, Springer Science and Business Media, New York, NY, 2013.

Wang, F., Guo, J., Wu, Y., Zhang, X., Deng, M., Li, X., Zhang, J., and Zhao, J.: Satellite observed aerosol-induced variability in warm cloud properties under different meteorological conditions over eastern China, Atmos. Environ., 84, 122–132, doi:10.1016/j.atmosenv.2013.11.018, 2014.

Warneke, C., Bahreini, R., Brioude, J., Brock, C. A., De Gouw, J. A., Fahey, D. W., Froyd, K. D., Holloway, J. S., Middlebrook, A., Miller, L., Montzka, S., Murphy, D. M., Peischl, J., Ryerson, T. B., Schwarz, J. P., Spademan, J. R., and Veres, P.: Biomass burning in Siberia and Kazakhstan as an important source for haze over the Alaskan Arctic in April 2008, Geophys. Res. Lett., 36, 2–7, doi:10.1029/2008GL036194, 2009.

Weisz, E., Li, J., Menzel, W. P., Heidinger, A. K., Kahn, B. H., and Liu, C. Y.: Comparison of AIRS, MODIS, CloudSat and CALIPSO cloud top height retrievals, Geophys. Res. Lett., 34, 1–5, doi:10.1029/2007GL030676, 2007.

Wesslén, C., Tjernström, M., Bromwich, D. H., De Boer, G., Ekman, A. M. L., Bai, L. S., and Wang, S. H.: The Arctic summer atmosphere: An evaluation of reanalyses using ASCOS data, Atmos. Chem. Phys., 14, 2605–2624, doi:10.5194/acp-14-2605-2014, 2014.

Westerling, A. L., Hidalgo, H. G., Cayan, D. R., and Swetnam, T. W.: Warming and earlier spring increase western U. S. forest wildfire activity, Science (New York, N. Y.), 313, 940–943, doi:10.1126/science.1128834, 2006.

Yoshimori, M., Watanabe, M., Abe-Ouchi, A., Shiogama, H., and Ogura, T.: Relative contribution of feedback processes to Arctic amplification of temperature change in MIROC GCM, Clim. Dynam., 42, 1613–1630, doi:10.1007/s00382-013-1875-9, 2013.

Zhao, C. and Garrett, T. J.: Effects of Arctic Haze on surface Cloud radiative forcing, Geophys. Res. Lett., 42, 557–564, doi:10.1002/2014GL062015, 2015.

Zhao, C., Klein, S. A., Xie, S., Liu, X., Boyle, J. S., and Zhang, Y.: Aerosol first indirect effects on non-precipitating low-level liquid cloud properties as simulated by CAM5 at ARM sites, Geophys. Res. Lett., 39, 1–7, doi:10.1029/2012GL051213, 2012.

Zygmuntowska, M., Mauritsen, T., Quaas, J., and Kaleschke, L.: Arctic clouds and surface radiation-a critical comparison of satellite retrievals and the ERA-interim reanalysis, Atmos. Chem. Phys., 12, 6667–6677, doi:10.5194/acp-12-6667-2012, 2012.

Table 1. Cloud products, pollution tracer, atmospheric reanalysis used in this study with the corresponding spatial and temporal resolution.

Parameter(s)	From:	Resolution(s)
Cloud parameter (T, r_e, τ)	MODIS, POLDER-3	Spatial resolution: $36\,\mathrm{km}^2$
CO tracer concentration from anthropogenic sources	FLEXPART	Spatial resolution: $1^\circ \times 2^\circ$, Temporal resolution: $3\,\mathrm{h}$
Specific humidity, temperature profile	ERA-I (ECMWF)	Spatial resolution: $1.5^\circ \times 1.5^\circ$, Temporal resolution: $6\,\mathrm{h}$

Table 2. Summary of the different ranges of the logarithm of the specific humidity and the LTS over the region of interest, detailing the method used to determine the final range of parameters considered. The Δ defines the difference between the maximum and the minimum of the total range. The considered range is chosen to keep the maximum number of measurements within a fixed interval of 15 % of the range, corresponding to the red square on Fig. 4.

	$\log_{10}$ (Specific Humidity)	LTS (°)
Total Range [Min, Max]	[−0.89, 1.0]	[2.1, 38]
Δ Total Range	1.9	36
15 % Interval	0.28	5.4
Controlled Range [Min, Max]	[0.30, 0.60] = [2.0, 4.0] ($\mathrm{g\,kg^{-1}}$)	[17, 22]

Table 3. PCI parameter calculated for the optical depth and the effective radius considering all clouds, graybody clouds and blackbody clouds, averaged from values presented in Fig. 5 and weighted considering the inverse of the uncertainty in the mean.

	All LWP	Graybody	Blackbody
PCI_{r_e}	0.12	0.10	0.14
PCI_{τ}	0.16	0.13	0.17

Table 4. PCI parameter calculated for the optical depth and the effective radius considering all clouds, graybody clouds, and blackbody clouds, for two different regimes of CO concentration representing lower and upper quartiles of CO concentration.

	All LWP		Graybody		Blackbody	
	PCI_{r_e}	PCI_{τ}	PCI_{r_e}	PCI_{τ}	PCI_{r_e}	PCI_{τ}
$\chi_{\mathrm{CO}} < 5.5\,\mathrm{ppbv}$	0.23	0.36	0.31	0.26	0.28	0.24
$\chi_{\mathrm{CO}} > 10\,\mathrm{ppbv}$	0.09	0.35	0.09	0.16	0.14	0.16

Table 5. Percentile values of specific humidity and LTS used to defined different regimes of the meteorological parameters.

	Specific Humidity ($\mathrm{g\,kg^{-1}}$)	LTS (K)
Minimum	0.13	2.1
20th percentile	1.2	14
40th percentile	1.7	18
60th percentile	2.4	20
80th percentile	3.6	23
Maximum	11	37

Table 6. Difference between PCI_{τ} and PCI_{r_e} (i.e. $\mathrm{PCI}_{\mathrm{LWP}}$) for graybody, blackbody, and all clouds when lower tropospheric stability and specific humidity are controlled and when they are not controlled. The averaged PCI values are shown in Table 3.

	All LWP	Graybody	Blackbody
Controlled	0.04	0.03	0.04
Not controlled	0.12	0.04	0.08

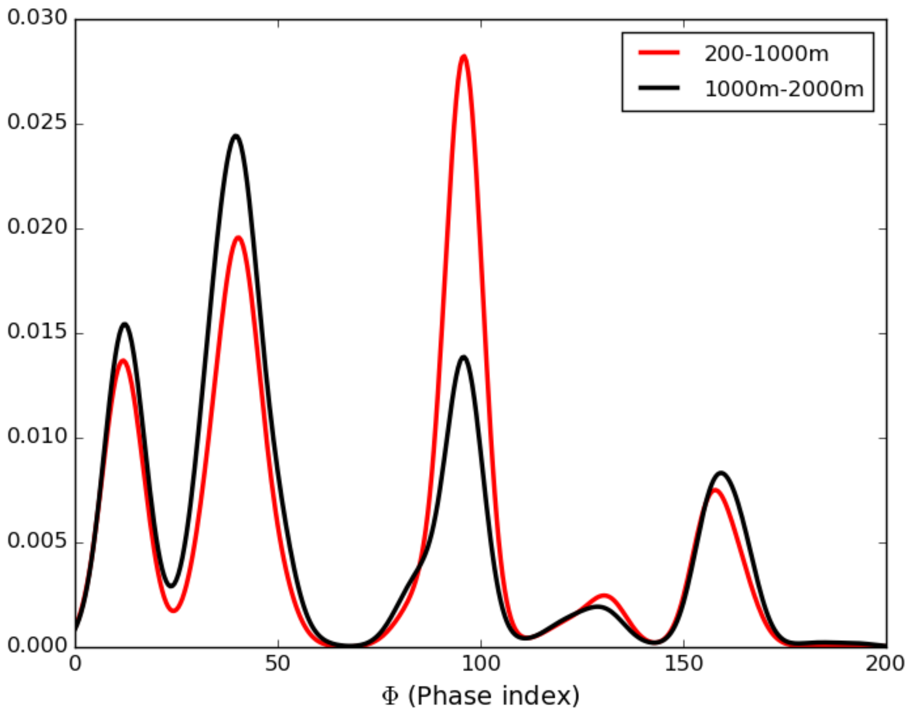

Figure 1. Normalized cloud thermodynamic phase index frequency distribution from the POLDER-MODIS algorithm, for pixels with the phase-index SD less than 10. Colors represent different cloud altitudes, between 200–1000 m in red and between 1000–2000 m in black.

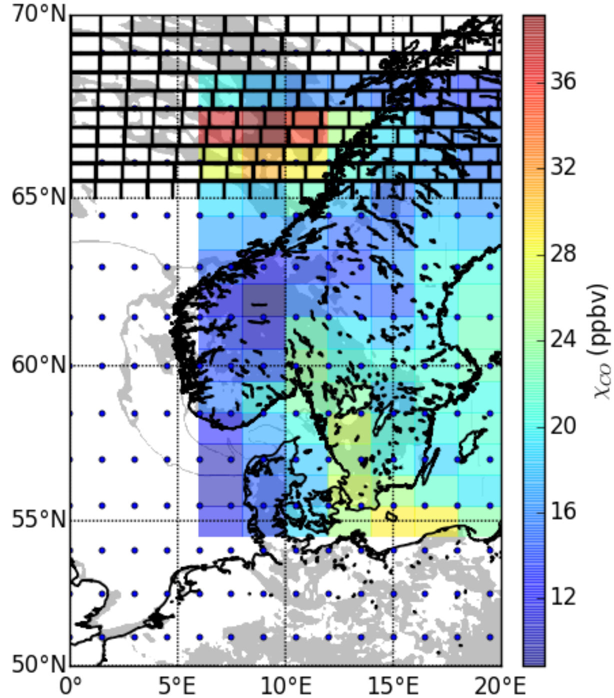

Figure 2. Illustration of the horizontal co-location method, showing satellite data corresponding to cloud top pressures below 1000 m altitude (gray shading), the average FLEXPART CO concentration between 1 and 2 km (colored shading), and the spatial resolution of temperature profiles and specific humidity in blue points. The black grid, at the top of the map, corresponds to the sinusoidal equal-area grid used in this study for co-locating each data set.

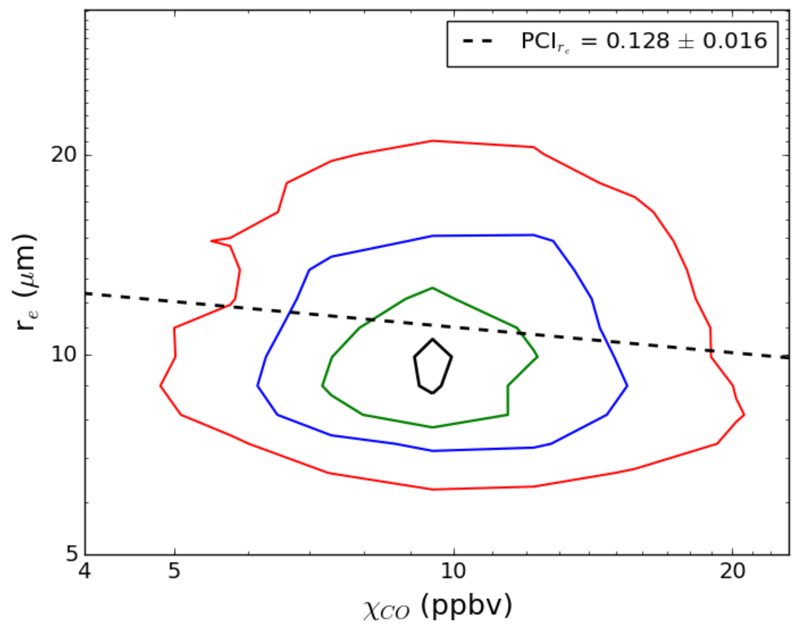

Figure 3. Calculation of the PCI parameter from a probability distribution of values in the effective radius and CO tracer concentration for liquid clouds with cloud top altitudes between 1000 m and 2000 m, and cloud top temperatures between -12 and 6.0 °C. The color scale indicates higher density of values in linear intervals. The PCI number indicates the negative slope of the linear fit (dashed line).

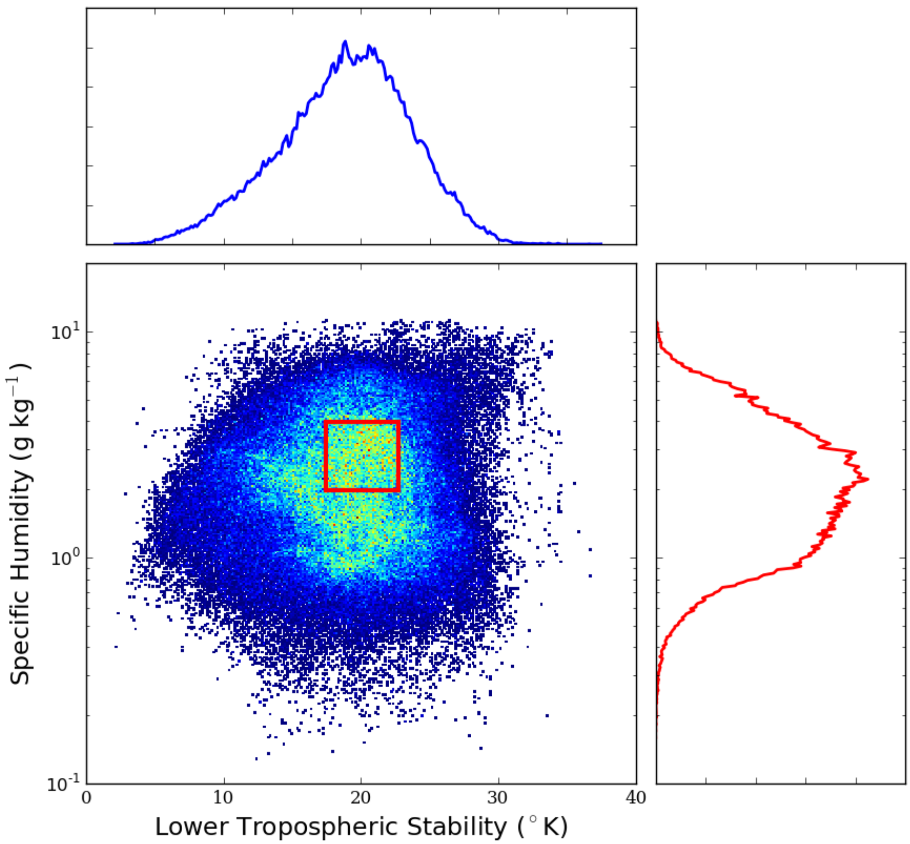

Figure 4. 2-D histogram of the specific humidity and the LTS retrieved by ECMWF reanalysis from 2008 to 2010. The red rectangle corresponds to the range where there is a maximum of measurements within a bin corresponding to 15 % of the total range length of the corresponding parameter.

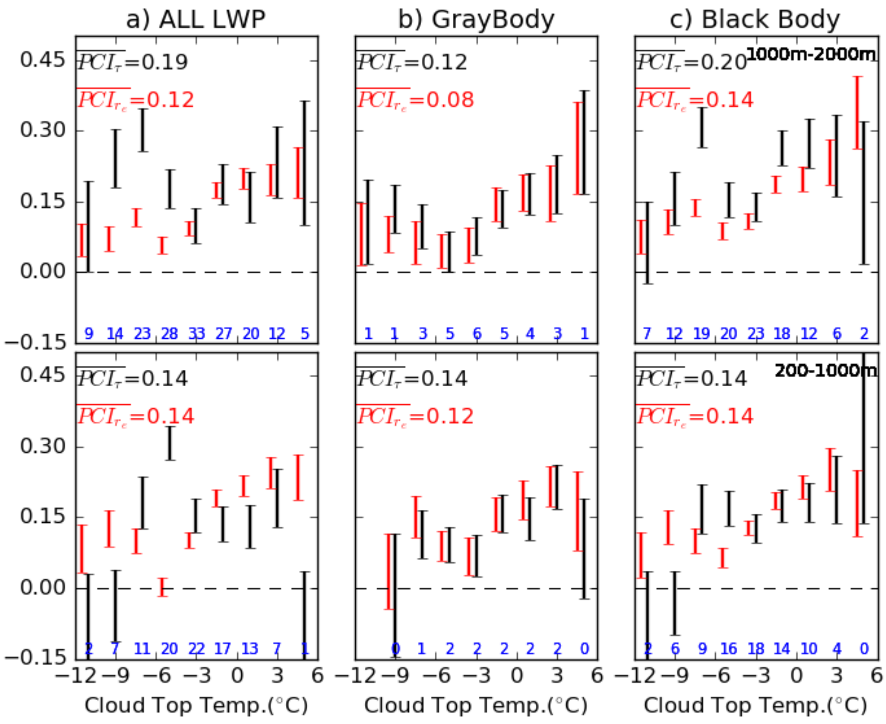

Figure 5. PCI parameter of the effective radius (r_e) (red) and optical depth (τ) (black), as a function of temperature calculated for liquid clouds between 200–1000 m (lower row) and 1000–2000 m (upper row). The bars indicate the 95 % confidence limit in the calculation of the mean PCI value. Each column corresponds to different thresholds for LWP (blackbody: LWP $> 40\,\mathrm{g\,m^{-2}}$, graybody: LWP $< 40\,\mathrm{g\,m^{-2}}$). Blue numbers indicate the number of grid-cells, in hundreds, that are used to calculate each PCI value. In each figure the PCI value averaged over the temperature and weighted according the inverse of the uncertainty is indicated.

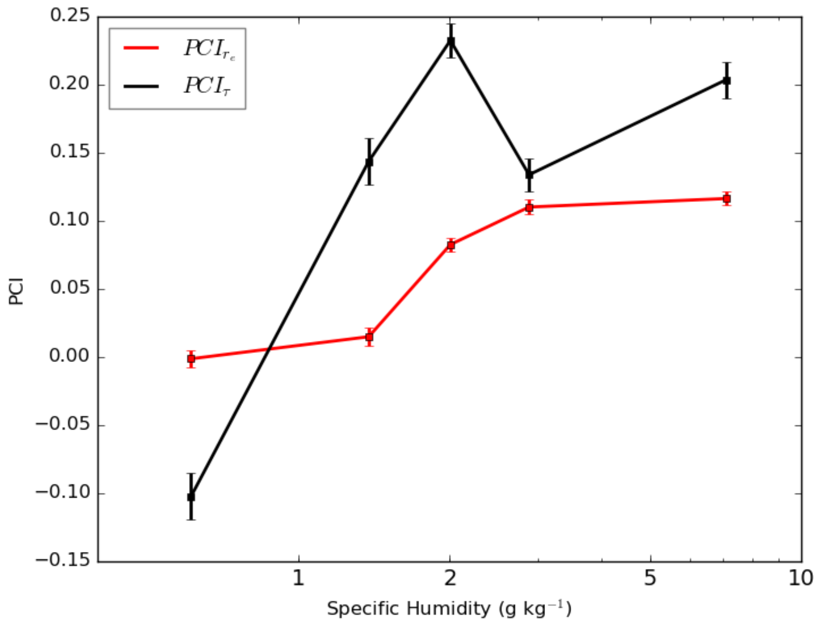

Figure 6. $\mathrm{PCI}_{r_\mathrm{e}}$ (red) and PCI_{τ} (black) for different bins of the specific humidity, controlled with values of LTS between 17 and 22 K. Each marker is placed in the middle of the corresponding bin.

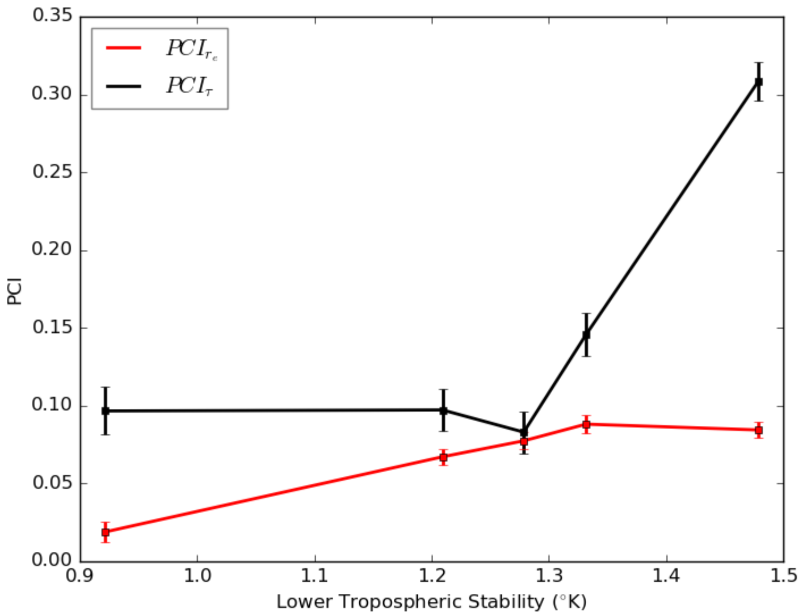

Figure 7. PCI_{r_e} (red) and PCI_{τ} (black) and PCI_{τ} as a function of the lower tropospheric stability, controlled with values of specific humidity between 2.0 and 4.0 $\mathrm{g\,kg^{-1}}$.

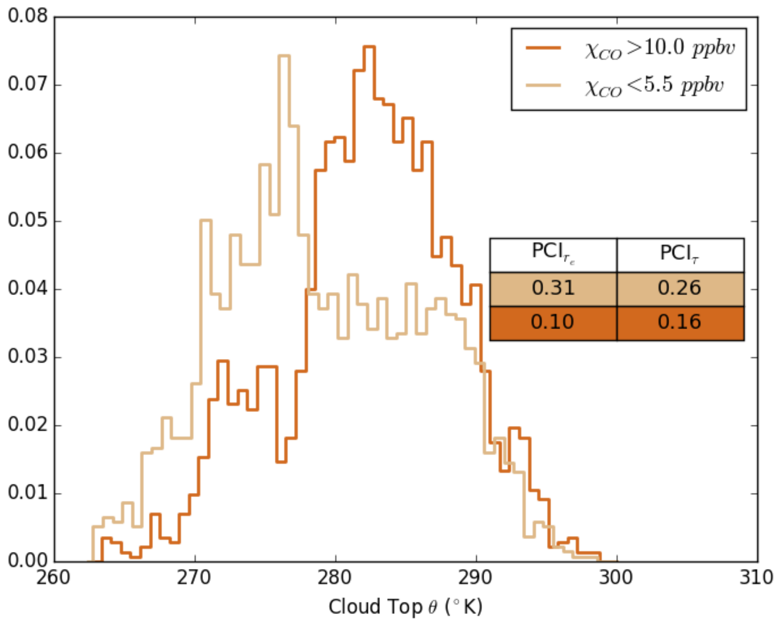

Figure 8. Normalized distribution of the cloud top potential temperature when clouds are associated with CO tracer concentrations (χ_{CO}) greater than 10 ppbv and less than 5 ppbv. The values of PCI$_{r_e}$ and PCI$_{\tau}$ associated with each histogram are presented also in Table 3.